High-field QCPMG-MAS NMR of halt-onteger quadropolar nuclei with large quadrupole couplings

Larsen, Flemming Hofmann; Jakobsen, Hans J.; Ellis, Paul D.; Nielsen, Niels Chr.

Published in:
Molecular Physics

Publication date:
1998

Document version
Early version, also known as pre-print

Citation for published version (APA):
Larsen, F. H., Jakobsen, H. J., Ellis, P. D., & Nielsen, N. C. (1998). High-field QCPMG-MAS NMR of halt-onteger quadropolar nuclei with large quadrupole couplings. *Molecular Physics*, *95*(6), 1185-1195.

MOLECULAR PHYSICS, 1998, VOL. 95, NO. 6, 1185–1195

High-field QCPMG-MAS NMR of half-integer quadrupolar nuclei with large quadrupole couplings

FLEMMING H. LARSEN[1,2], HANS J. JAKOBSEN[1], PAUL D. ELLIS[2] and
NIELS CHR. NIELSEN[1]

[1] Instrument Centre for Solid-State NMR Spectroscopy, Department of Chemistry,
University of Aarhus, DK-8000 Aarhus C, Denmark
[2] Environmental Molecular Sciences Laboratory, Pacific Northwest National
Laboratory, Richland, WA 99352, USA

(*Received 15 May 1998; accepted 1 July 1998*)

The quadrupole Carr–Purcell–Meiboom–Gill NMR experiment using magic-angle spinning (QCPMG-MAS) is analysed as a means of determining quadrupolar coupling and anisotropic chemical shielding tensors for half-integer ($I > 1/2$) quadrupolar nuclei with large quadrupole coupling constants (C_Q). This is accomplished by numerical simulations and ^{87}Rb NMR experiments wih Rb_2SO_4 and Rb_2CrO_4 using different magnetic fields. It is demonstrated that (i) QCPMG-MAS experiments typically provide a sensitivity gain by more than an order of magnitude relative to quadrupolar-echo MAS experiments, (ii) non-secular second-order terms do not affect the spin evolution appreciably, and (iii) the effect of finite RF pulses needs to be considered when $2\omega_Q^2/(\omega_0\omega_{RF}) > 0.1$, where $\omega_Q = 2\pi C_Q/(4I(2I-1))$, ω_{RF} is the RF amplitude, and ω_0 the Larmor frequency. Using numerical simulations and iterative fitting the magnitudes and relative orientation of ^{87}Rb quadrupolar coupling and chemical shielding tensors for Rb_2SO_4 and Rb_2CrO_4 have been determined.

1. Introduction

Parameters for quadrupolar coupling and anisotropic chemical shielding interactions determined by solid-state nuclear magnetic resonance (NMR) spectroscopy have long been recognized as useful probes of local structure and dynamics in solids. Tensors for the two interactions provide detailed and complementary information about the local electronic environment for quadrupolar ($I > 1/2$) nuclei. This includes, for example, important information about local symmetry which is difficult to access by other means. During the past decade these aspects have motivated the development and application of numerous experimental methods. Among these should be mentioned nutation NMR [1–3], detection of satellite transitions by magic-angle spinning (MAS) [4, 5], dynamic-angle spinning (DAS) [6], double rotation (DOR) [7–9], switched-angle spinning (SAS) [10], multiple-quantum (MQ) MAS [11–14], and single-crystal NMR [15, 16]. In general these methods work well in cases of relatively small quadrupolar coupling constants (C_Q). Upon going to larger C_Q's, however, the powder experiments become increasingly difficult to perform and generally suffer from low sensitivity when relying on state-of-the-art sample spinning frequencies and static magnetic and radiofrequency (RF) field strengths [17, 18]. In this case the quadrupole-echo (QE) method [19–21] traditionally has been regarded as the method of choice for detecting the rapidly decaying free-induction decay (FID) without disturbance from finite receiver dead time and probe ringing.

For half-integer quadrupolar nuclei with large C_Q values even QE or QE-MAS experiments suffer from low sensitivity and resolution, since the second-order quadrupolar powder pattern of the central transition can be several hundred kHz wide. Furthermore, it becomes increasingly difficult to distinguish wide, low-sensitivity spinning sideband patterns from the baseline, which may hamper extraction of information about, e.g., anisotropic chemical shielding. To remedy these problems, while maintaining structural or dynamic information from the anisotropic interactions, we recently introduced static [22], MAS [23], and MQ-MAS [14] versions of the quadrupolar Carr–Purcell–Meiboom–Gill (QCPMG) [24, 25] experiment sampling the FID in the course of a train of π pulses operating selectively on the central transition. In this manner the second-order powder pattern of the central transition is split into manifolds of spin–echo sidebands. This leads to a huge increase in sensitivity compared with the corresponding QE and QE-MAS experiments, and facilitates unambiguous distinction between baseline and real signals.

In particular the QCPMG-MAS experiment, taking advantage of partial averaging of the second-order quadrupolar coupling by fast MAS, appears promising for studying half-integer quadrupolar nuclei with large C_Q's. In cases where the line broadening is dominated by second-order quadrupole coupling, an additional gain in sensitivity and resolution may be expected by performing the QCPMG-MAS experiments under high magnetic fields. Furthermore, this scales up the chemical shielding interaction, which may be of interest when studying combined effects from chemical shielding and quadrupolar coupling tensors.

Although QCPMG-MAS NMR for sensitivity reasons represents a promising method for studying nuclei with large quadrupolar couplings, it is important to keep in kind that it relies on multiple-pulse RF irradiation, which may be disturbed by dominant anisotropic interactions. Therefore, for large C_Q's the influence of finite RF pulse irradiation needs to be considered in order to extract reliable parameters for the anisotropic interactions. Furthermore, it is relevant to investigate the influence of non-secular terms of the second-order quadrupolar interaction which do not vanish in the high-field approximation. In the present work these important aspects for the applicability of QCPMG-MAS are examined theoretically and demonstrated experimentally by ^{87}Rb NMR of Rb_2SO_4 and Rb_2CrO_4.

2. Theory

In the Zeeman interaction representation, the evolution of the spin states for an ensemble of quadrupolar nuclei may to a good approximation be described by the high field truncated effective Hamiltonian

$$\bar{\mathcal{H}}(t) = \mathcal{H}_{\mathrm{RF}} + \bar{\mathcal{H}}_{\mathrm{int}}(t), \tag{1}$$

$$\bar{\mathcal{H}}_{\mathrm{int}}(t) = \bar{\mathcal{H}}_{\sigma}^{(1)}(t) + \bar{\mathcal{H}}_{\mathrm{Q}}^{(1)}(t) + \bar{\mathcal{H}}_{\mathrm{Q}}^{(2)}(t), \tag{2}$$

where

$$\mathcal{H}_{\mathrm{RF}} = \omega_{\mathrm{RF}}(I_x \cos\phi + I_y \sin\phi), \tag{3}$$

$$\bar{\mathcal{H}}_{\sigma}^{(1)}(t) = -\omega_0\left(R^{\sigma}_{0,0}T^{\sigma}_{0,0} + (R^{\sigma}_{2,0})^{\mathrm{L}}T^{\sigma}_{2,0}\right), \tag{4}$$

$$\bar{\mathcal{H}}_{\mathrm{Q}}^{(1)}(t) = 2\omega_{\mathrm{Q}}(R^{\mathrm{Q}}_{2,0})^{\mathrm{L}}T^{\mathrm{Q}}_{2,0}, \tag{5}$$

$$\begin{aligned}\bar{\mathcal{H}}_{\mathrm{Q}}^{(2)}(t) = -\frac{2\omega_{\mathrm{Q}}^2}{\omega_0}\Big(&(R^{\mathrm{Q}}_{2,-2})^{\mathrm{L}}(R^{\mathrm{Q}}_{2,2})^{\mathrm{L}}[T^{\mathrm{Q}}_{2,2}, T^{\mathrm{Q}}_{2,-2}]\\ &+ (R^{\mathrm{Q}}_{2,0})^{\mathrm{L}}(R^{\mathrm{Q}}_{2,2})^{\mathrm{L}}[T^{\mathrm{Q}}_{2,-2}, T^{\mathrm{Q}}_{2,0}]\\ &+ (R^{\mathrm{Q}}_{2,-2})^{\mathrm{L}}(R^{\mathrm{Q}}_{2,0})^{\mathrm{L}}[T^{\mathrm{Q}}_{2,0}, T^{\mathrm{Q}}_{2,2}]\\ &- 2(R^{\mathrm{Q}}_{2,0})^{\mathrm{L}}(R^{\mathrm{Q}}_{2,1})^{\mathrm{L}}[T^{\mathrm{Q}}_{2,-1}, T^{\mathrm{Q}}_{2,0}]\\ &+ 2(R^{\mathrm{Q}}_{2,-1})^{\mathrm{L}}(R^{\mathrm{Q}}_{2,1})^{\mathrm{L}}[T^{\mathrm{Q}}_{2,1}, T^{\mathrm{Q}}_{2,-1}]\\ &- 2(R^{\mathrm{Q}}_{2,-1})^{\mathrm{L}}(R^{\mathrm{Q}}_{2,0})^{\mathrm{L}}[T^{\mathrm{Q}}_{2,0}, T^{\mathrm{Q}}_{2,1}]\Big),\end{aligned} \tag{6}$$

describe RF irradiation of amplitude $\omega_{\mathrm{RF}} = -\gamma B_{\mathrm{RF}}$ and phase ϕ ($\mathcal{H}_{\mathrm{RF}}$), chemical shielding to first order $\bar{\mathcal{H}}_{\sigma}^{(1)}$), secular terms of the first-order quadrupolar interaction ($\bar{\mathcal{H}}_{\mathrm{Q}}^{(1)}$), and secular as well as non-secular terms of the second-order quadrupolar interaction ($\bar{\mathcal{H}}_{\mathrm{Q}}^{(2)}$). These terms are relevant in the regime of $|\mathcal{H}_{\mathrm{Q}}| \gg |\mathcal{H}_{\sigma}|$. The constants $\omega_0 = -\gamma B_0$, $C_{\mathrm{Q}} = e^2qQ/h$, I, and $\omega_{\mathrm{Q}} = 2\pi C_{\mathrm{Q}}/(4I(2I-1))$ denote the Larmor frequency, the quadrupole coupling constant, the spin-quantum number, and the maximum quadrupole splitting, respectively.

In equations (4)–(6) the spin and spatial parts of the internal Hamiltonian are expressed in terms of jth rank irreducible tensor operators $T^{\lambda}_{j,m}$ and $R^{\lambda}_{j,m}$, respectively ($\lambda = \sigma, \mathrm{Q}$). For the spin part these operators are related to Cartesian operators according to

$$T^{\sigma}_{0,0} = \left(\frac{3}{2}\right)^{1/2} T^{\sigma}_{2,0} = I_z, \tag{7}$$

$$T^{\mathrm{Q}}_{2,0} = \frac{1}{6^{1/2}}(3I_z^2 - I(I+1)), \tag{8}$$

$$[T^{\mathrm{Q}}_{2,1}, T^{\mathrm{Q}}_{2,-1}] = \frac{1}{2}I_z(4I(I+1) - 8I_z^2 - 1), \tag{9}$$

$$[T^{\mathrm{Q}}_{2,2}, T^{\mathrm{Q}}_{2,-2}] = I_z(2I(I+1) - 2I_z^2 - 1), \tag{10}$$

$$[T^{\mathrm{Q}}_{2,\pm1}, T^{\mathrm{Q}}_{2,0}] = \mp\left(\frac{3}{8}\right)^{1/2}(4I_z^2 \mp 4I_z + 1)I_{\pm}, \tag{11}$$

$$[T^{\mathrm{Q}}_{2,\pm2}, T^{\mathrm{Q}}_{2,0}] = \mp 6^{1/2}(I_z \mp 1)I_{\pm}^2. \tag{12}$$

The time-dependent spatial tensors $(R^{\lambda}_{j,m})^{\mathrm{L}}$ in the laboratory frame (L) may be described conveniently using

$$\left(\frac{2}{3}\right)^{1/2}\omega_0(R^{\sigma}_{2,0})^{\mathrm{L}} = \sum_{m=-2}^{2}\omega_{\sigma}^{(m)}\exp\{-\mathrm{i}m(\omega_{\mathrm{r}}t + \gamma_{\mathrm{CR}})\} \tag{13}$$

$$\left(\frac{2}{3}\right)^{1/2}\omega_{\mathrm{Q}}(R^{\mathrm{Q}}_{2,0})^{\mathrm{L}} = \sum_{m=-2}^{2}\omega_{\mathrm{Q1}}^{(0,m)}\exp\{-\mathrm{i}m(\omega_{\mathrm{r}}t + \gamma_{\mathrm{CR}})\} \tag{14}$$

$$-\frac{2\omega_{\mathrm{Q}}^2}{\omega_0}(R^{\mathrm{Q}}_{2,-p})^{\mathrm{L}}(R^{\mathrm{Q}}_{2,p})^{\mathrm{L}} = \sum_{m=-4}^{4}\omega_{\mathrm{Q2}}^{(m,p)}\exp\{-\mathrm{i}m(\omega_{\mathrm{r}}t + \gamma_{\mathrm{CR}})\}, \tag{15}$$

with the Fourier components

$$\omega_{\sigma}^{(m)} = \left(\frac{2}{3}\right)^{1/2} \omega_0 \sum_{m''=-2}^{2} \sum_{m'=-2}^{2} (R^{\sigma}_{2,m''})^{\mathrm{P}} \mathbf{D}^{(2)}_{m'',m'}(\Omega^{\sigma}_{\mathrm{PC}}) \times \mathbf{D}^{(2)}_{m',m}(\Omega_{\mathrm{CR}}) \mathbf{d}^{(2)}_{m,0}(\beta_{\mathrm{RL}}) \tag{16}$$

$$\omega_{\mathrm{Q1}}^{(m,p)} = \left(\frac{2}{3}\right)^{1/2} \omega_{\mathrm{Q}} \sum_{m'=-2}^{2} (R^{\mathrm{Q}}_{2,m'})^{\mathrm{P}} \mathbf{D}^{(2)}_{m',m}(\Omega_{\mathrm{CR}}) \times \mathbf{d}^{(2)}_{m,p}(\beta_{\mathrm{RL}}), \tag{17}$$

$$\omega_{\mathrm{Q2}}^{(m,p)} = -\frac{3}{\omega_0} \sum_{m'=-2}^{2} \omega_{\mathrm{Q1}}^{(m',p)} \omega_{\mathrm{Q1}}^{(m-m',-p)}, \tag{18}$$

where the summation in equation (18) is defined for $(m - m') \in \{-2,-1,0,1,2\}$. The non-vanishing principal-axis frame tensor elements are given by $(R^{\sigma}_{0,0})^{\mathrm{P}} = \delta_{\mathrm{iso}}$, $(R^{\sigma}_{2,0})^{\mathrm{P}} = (3/2)^{1/2}\delta_{\sigma}$, $(R^{\sigma}_{2,\pm 2})^{\mathrm{P}} = -\eta_{\sigma}\delta_{\sigma}/2$, $(R^{\mathrm{Q}}_{2,0})^{\mathrm{P}} = (3/2)^{1/2}$, and $(R^{\mathrm{Q}}_{2,\pm 2})^{\mathrm{P}} = -\eta_{\mathrm{Q}}/2$ where $\delta_{\sigma} = \delta_{zz} - \delta_{\mathrm{iso}}$, $\lambda_{\mathrm{iso}} = (\lambda_{xx} + \lambda_{yy} + \lambda_{zz})/3$, and

$$\eta_{\lambda} = (\lambda_{yy} - \lambda_{xx})/(\lambda_{zz} - \lambda_{\mathrm{iso}})$$

using the ordering

$$|\lambda_{zz} - \lambda_{\mathrm{iso}}| \geq |\lambda_{yy} - \lambda_{\mathrm{iso}}| \geq |\lambda_{xx} - \lambda_{\mathrm{iso}}|$$

$(\lambda = \sigma, \mathrm{Q})$.

Transformation of the spatial tensor from its principal axis frame (P), through a crystal-fixed frame (C) and a rotor-fixed frame (R), into the laboratory frame (L) is described by Wigner rotation matrices $\mathbf{D}^{(2)}(\Omega_{XY})$ with the Euler angles $\Omega_{XY} = \{\alpha_{XY}, \beta_{XY}, \gamma_{XY}\}$ relating frames X and Y. For convenience C is chosen to coincide with the principal-axis frame of the quadrupolar coupling tensor (i.e., $\Omega^{\mathrm{Q}}_{\mathrm{PC}} = \{0,0,0\}$) implying that the relative orientation of the quadrupolar coupling and anisotropic shielding tensors are given by

$$\Omega^{\sigma}_{\mathrm{PC}} = \{\alpha^{\sigma}_{\mathrm{PC}}, \beta^{\sigma}_{\mathrm{PC}}, \gamma^{\sigma}_{\mathrm{PC}}\}.$$

We note the ambiguity $\alpha^{\sigma}_{\mathrm{PC}} = \alpha^{\sigma}_{\mathrm{PC}} + n\pi$ and

$$\gamma^{\sigma}_{\mathrm{PC}} = \gamma^{\sigma}_{\mathrm{PC}} + m\pi$$

with n and m being arbitrary integers and that the QCPMG-MAS spectrum is independent of $\alpha^{\sigma}_{\mathrm{PC}}$ and $\gamma^{\sigma}_{\mathrm{PC}}$ in the special cases $\eta_{\sigma} = 0$ and $\eta_{\mathrm{Q}} = 0$, respectively. $\Omega_{\mathrm{CR}} = \{\alpha_{\mathrm{CR}}, \beta_{\mathrm{CR}}, 0\}$ includes two of the powder angles (γ_{CR} is part of the exponents in equations (13)–(15)) while $\beta_{\mathrm{RL}} = \cos^{-1}(1/3^{1/2})$ and $\omega_{\mathrm{r}}/2\pi$ denotes the magic angle distinguishing the rotor axis from the field direction and the spinning speed, respectively. $\mathbf{d}^{(2)}(\beta_{\mathrm{RL}})$ is a reduced Wigner matrix.

Using equations (1)–(6), it is possible to calculate the response of an ensemble of quadrupolar nuclei to the QCPMG-MAS pulse sequence reproduced in figure 1.

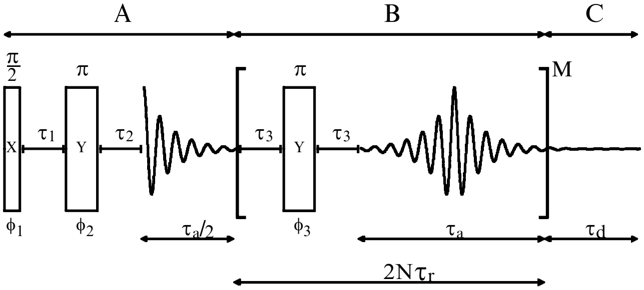

Figure 1. QCPMG-MAS pulse sequence. Following a solid echo with sampling of the first half-echo (part A), the subsequent part of the FID is sampled during a rotor-synchronized train of π pulses (part B) ending with an extended acquisition period (part C) to ensure full decay of the FID. For half-integer quadrupolar nuclei with large quadrupole couplings, the nominal pulse flip angles (indicated above the pulses) are scaled by $(I + \frac{1}{2})^{-1}$. Rotor synchronization requires $\tau_1 = \tau_{\mathrm{r}} - \tau_{\pi/2}$ and $2N\tau_{\mathrm{r}} = \tau_a + 2\tau_3 + \tau_{\pi}$ where N is an integer, τ_{r} the rotor period, and $\tau_{\pi/2}$ and τ_{π} durations of selective π/2 and π pulses. τ_2 is adjusted to start the acquisition at an echo maximum. The pulse phases ϕ_1, ϕ_2, and ϕ_3 are given in [22].

Following a rotor synchronized QE with sampling of the decaying half of the echo (part A), the remaining part of the FID is sampled during part B interrupted by rotor synchronized π refocusing pulses and ending with a final extended free precession period (part C) to ensure full decay of the FID. Within the secular approximation evolution during periods of free precession (subscript f) and during periods of RF irradiation (subscript ϕ referring to the phase of the pulse) is governed by the propagators

$$\tilde{U}_{\mathrm{f}}(t_2, t_1) = \exp\left\{-\mathrm{i}\int_{t_1}^{t_2} \overline{\mathcal{H}}_{\mathrm{int}}(t)\mathrm{d}t\right\}, \tag{19}$$

$$\tilde{U}_{\phi}(t_2, t_1) = T\exp\left\{-\mathrm{i}\int_{t_1}^{t_2} \overline{\mathcal{H}}(t)\mathrm{d}t\right\}, \tag{20}$$

where T is the Dyson time-ordering operator [26] necessary since $[\overline{\mathcal{H}}_{\mathrm{int}}(t'), \overline{\mathcal{H}}_{\mathrm{int}}(t'')] \neq 0$. We note that $\overline{\mathcal{H}}_{\mathrm{int}}(t)$ and $\overline{\mathcal{H}}(t)$ in the usual Zeeman base adopt diagonal and tridiagonal forms, respectively. $\tilde{U}_{\mathrm{f}}(t_2, t_1)$ may be calculated readily by direct integration while $\tilde{U}_{\phi}(t_2, t_1)$ conveniently may be obtained as a time-ordered product of propagators, i.e.:

$$\tilde{U}_{\phi}(t_2, t_1) = \exp\{-\mathrm{i}\overline{\mathcal{H}}(t_1 + N\Delta t)\Delta t\} \times \cdots \times \exp\{-\mathrm{i}\overline{\mathcal{H}}(t_1 + \Delta t)\Delta t\}, \tag{21}$$

where $\Delta t = (t_2 - t_1)/N$ is a short time period over which the Hamiltonian may be considered approximately time independent. When non-secular terms are included, propagators for periods of free precession also are tridiagonal and therefore calculated using Dyson time ordering.

Equipped with equations (19)–(21), it is straightforward to calculate the propagator corresponding to any point in time in the rotor-synchronized QCPMG-MAS pulse sequence. For example, the propagator corresponding to the first point in the FID is calculated for one crystalline orientation as

$$\begin{aligned}\tilde{U}(3\tau_{\pi/2}+2\tau_1,0) &= \tilde{U}_{\mathrm{f}}(3\tau_{\pi/2}+\tau_2+\tau_1,3\tau_{\pi/2}+\tau_1)\\ &\quad\times\tilde{U}_{\pi/2}(3\tau_{\pi/2}+\tau_1,\tau_{\pi/2}+\tau_1)\\ &\quad\times\tilde{U}_{\mathrm{f}}(\tau_{\pi/2}+\tau_1,\tau_{\pi/2})\tilde{U}_0(\tau_{\pi/2},0),\end{aligned}\qquad(22)$$

with the timings defined in the caption of figure 1. Upon averaging over all uniformly distributed crystallite orientations the detected signal may be described as

$$\begin{aligned}s(t) &= \frac{1}{8\pi^2}\int_0^{2\pi}\mathrm{d}\alpha_{\mathrm{CR}}\int_0^{\pi}\sin(\beta_{\mathrm{CR}})\mathrm{d}\beta_{\mathrm{CR}}\int_0^{2\pi}\mathrm{d}\gamma_{\mathrm{CR}}\\ &\quad\times\mathrm{Tr}\{I^+\tilde{U}(t,0)I_z\tilde{U}^\dagger(t,0)\},\end{aligned}\qquad(23)$$

with the operators I_z and I^+ being representatives of the initial density operator and the 'observable' for quadrature detection. We note that the powder averaging is performed numerically by simple sums selecting the $\{\alpha_{\mathrm{CR}},\beta_{\mathrm{CR}}\}$ angles according to the tiling scheme of Zaremba [27] (details in [22]) and stepping the γ_{CR} angles equidistantly.

3. Effects from finite RF pulses and non-secular second-order terms

In simulation of QCPMG-MAS spectra for half-integer quadrupolar nuclei with large C_Q's, it is relevant to consider the effects from finite RF pulses and potentially also non-secular second-order terms of the quadrupole interaction. Addressing first the effect of finite RF pulses, it is known that in the relevant regime $|\omega_Q/\omega_{\mathrm{RF}}|>3$ the dominant first-order quadrupole interaction does not introduce any complicating effects to the RF performance on the central transition apart from uniform scaling of the nutation frequency by a factor $(I+\frac{1}{2})$ [3, 28, 29]. In the regime $0.2<|\omega_Q/\omega_{\mathrm{RF}}|<3$, ω_Q and ω_{RF} become sufficiently close in magnitude that the RF performance becomes more complicated and requires specific evaluation [3, 29]. Likewise, interference from the second-order quadrupolar coupling may be anticipated when $2\omega_Q^2/(\omega_0\omega_{\mathrm{RF}})>0.1$.

It was shown earlier that to a good approximation, for RF amplitudes fulfilling $|\omega_Q/\omega_{\mathrm{RF}}|>3$ and $2\omega_Q^2/(\omega_0\omega_{\mathrm{RF}})<0.1$, QCMPG-MAS spectra can be simulated within the assumption of ideal RF pulses [23]. For nuclei characterized by large C_Q's this condition cannot always be realized. As an example, consider an ensemble of spin $I=3/2$ nuclei with $C_Q=10\,\mathrm{MHz}$ and experimental conditions with $\omega_0/2\pi=-130\,\mathrm{MHz}$ and $\omega_{\mathrm{RF}}/2\pi=-65\,\mathrm{kHz}$. In this case $|\omega_Q/\omega_{\mathrm{RF}}|=12.8$ and $2\omega_Q^3/(\omega_0\omega_{\mathrm{RF}})=0.16$. The first value indicates that the QCPMG-MAS experiment with scaling of the pulse flip angles by $(I+\frac{1}{2})^{-1}$ will perform without noticeable complications from $\overline{\mathcal{H}}_Q^{(1)}$ while the second suggests interference from $\mathcal{H}_Q^{(2)}$. That this is indeed the case is demonstrated in figure 2 by comparison of QCPMG-MAS spectra calculated using the secular terms of the internal Hamiltonian

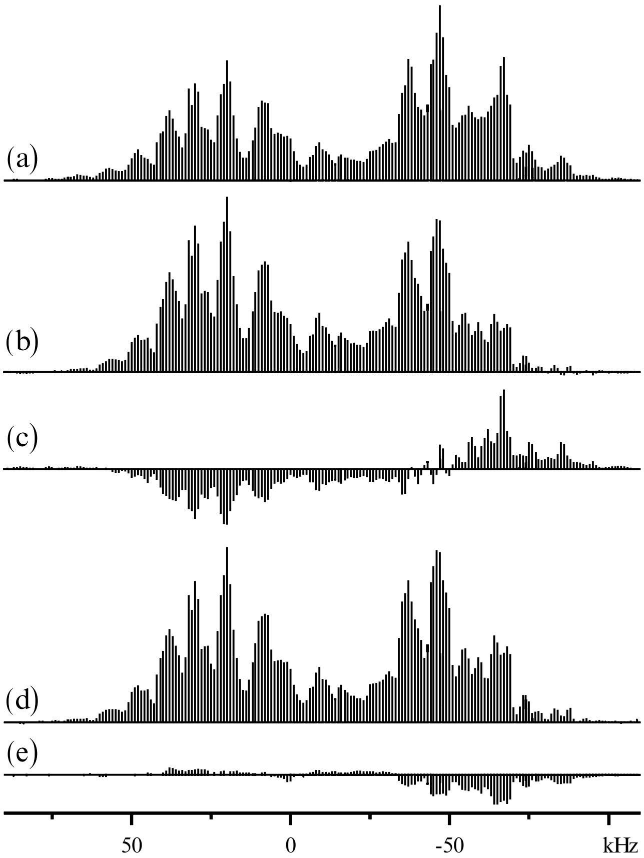

Figure 2. Theoretical QCPMG-MAS spectra illustrating the effect of finite RF pulses for a powder of quadrupolar nuclei characterized by $I=3/2$, $C_Q=10\,\mathrm{MHz}$, $\eta_Q=0.12$, $\delta_\sigma=150\,\mathrm{ppm}$, $\eta_\sigma=0.60$, $\delta_{\mathrm{iso}}=0.0\,\mathrm{ppm}$, and $\Omega_{PC}^{\sigma}=(90^\circ,30^\circ,90^\circ)$. Each spectrum represents a stick plot of integrated sideband intensities calculated using the experimental parameters $\omega_0/2\pi=-130.84\,\mathrm{MHz}$, $\omega_r/2\pi=9.5\,\mathrm{kHz}$, $\omega_{\mathrm{RF}}/2\pi=64.1\,\mathrm{kHz}$, $\tau_a=2.0\,\mathrm{ms}$, $\tau_d=3.14\,\mathrm{ms}$, $M=19$, and a dwell time of 4 μs under the assumption of (*a*) ideal and (*b*) finite RF pulses (see text). Spectrum (*d*) is obtained by calculating the FID resulting from an $M=1$ pulse sequence with finite RF pulses and replicating the part of the FID corresponding to part B of the pulse sequence to generate the full FID. (*c*) Difference between (*a*) and (*b*), and (*e*) difference between (*b*) and (*d*).

(*vide infra*) under the assumption of ideal (figure 2(*a*)) and finite (figure 2(*b*)) RF pulses. The relevance of considering the effects of finite RF pulses becomes particularly pronounced from the difference plot in figure 2(*c*).

Unfortunately, the improved QCPMG-MAS simulations considering finite RF pulses comes at a cost: the simulation in figure 2(*a*) requires 3.2 m in CPU time, but the corresponding simulation in figure 2(*b*) requires 186 m of CPU time. A major reason for the relatively fast simulations within the ideal RF pulse approach is that the FID may be generated by replication of the first full-echo envelope readily established by symmetrizing the half-echo from a sequence with $M = 0$ (cf. figure 1). Taking into account that typically the spectral simulations aim at extracting up to 8 parameters describing the magnitudes and relative orientations of quadrupolar coupling and anisotropic shielding tensors through iterative fitting, even the CPU time required for the ideal calculation is quite long. With an increase in CPU time by a factor of 60, considering finite RF pulses, iterative fitting appears outside practical reach. A similar problem was encountered earlier in a simulation of static-sample QCPMG spectra, in which case it proved possible to speed up finite RF pulse calculations by replicating part B of the FID [22]. Using a similar approach, figure 2(*d*) shows an approximated finite RF pulse QCPMG-MAS spectrum calculated within one tenth of the CPU time required for the spectrum in figure 2(*b*). Specifically, the spectrum in figure 2(*d*) was obtained by calculating the initial QE half-echo and the first spin–echo envelope of the repeating part B of the pulse sequence under consideration of finite RF pulses and subsequently replicating the latter part M times to form the remaining part of the FID. The favourable agreement between the 'numerically exact' spectrum in figure 2(*b*) and the approximated spectrum in figure 2(*d*) (difference plot in figure 2(*e*)) reveals that at least initial stages of iterative fitting may benefit greatly from the factor of ten in computation speed offered by replication.

Since the fastest approach to simulation and iterative fitting of experimental spectra still requires the assumption of ideal RF pulse, it is relevant to investigate the range of applicability of this approach. Figure 3 shows a series of typical QCPMG-MAS spectra calculated using anisotropic interaction parameters as in figure 2, $\omega_r/2\pi = 9.5$ kHz, and RF field strengths adjusted to fulfil $2\omega_Q^2/(\omega_o\omega_{RF}) = 0$ to 0.2 in steps of 0.05. These spectra reinforce that QCPMG-MAS spectra to a relatively good approximation may be calculated using the fast ideal RF pulse approach for $2\omega_Q^2/(\omega_0\omega_{RF})$ values up to about 0.1.

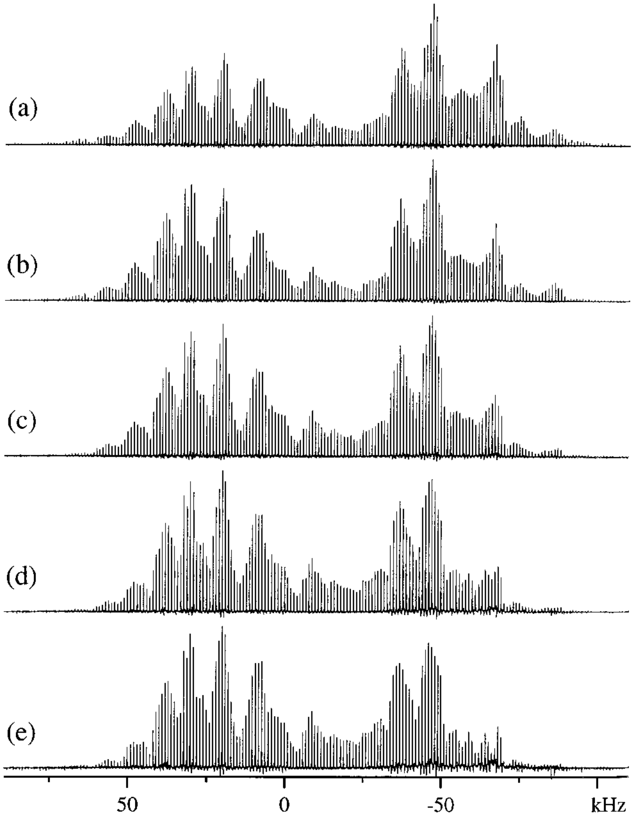

Figure 3. Theoretical QCPMG-MAS spectra calculated using parameters as in figure 2 but variation of $2\omega_Q^2/(\omega_0\omega_{RF})$ according to (*a*) 0.0 (ideal RF pulses), (*b*) 0.05 (213.7), (*c*) 0.1 (106.8), (*d*) 0.15 (71.2), and (*e*) 0.20 (53.4). Numbers in parentheses give the RF field strength ($\omega_{RF}/2\pi$) in kHz. Vertical scaling factors of (*a*) 1.0, (*b*) 3.4, (*c*) 3.7, (*d*) 4.5, and (*e*) 5.2 have been used. All spectra were weighted by a Lorentzian of 20 Hz linewidth.

To our knowledge, all previous studies involving second-order quadrupolar effects in powder spectra have *a priori* neglected influence from the non-secular second-order terms not truncated in the high field approximation. As judged from good agreement between experimental and simulated spectra, this may be an acceptable approximation in the case of free precession under the influence of weak to modest quadrupolar coupling interactions. However, the situation may be different for large C_Q's, especially when periods of finite RF pulse irradiation are involved. To explore this aspect, figure 4 compares QCPMG-MAS spectra calculated using the same parameters as in figure 3(*e*) (finite RF pulses) under consideration of secular (figure 4(*a*)) and secular as well as non-secular (figure 4(*b*)) contributions to the internal Hamiltonian as defined by equations (1)–(6). The vanishing difference (figure 4(*c*)) between these spectra suggests strongly that non-secular terms may safely be ignored in a simulation of typical QCPMG-MAS spectra. This is of significant practical value since simulation of the spectrum in figure 4(*b*)

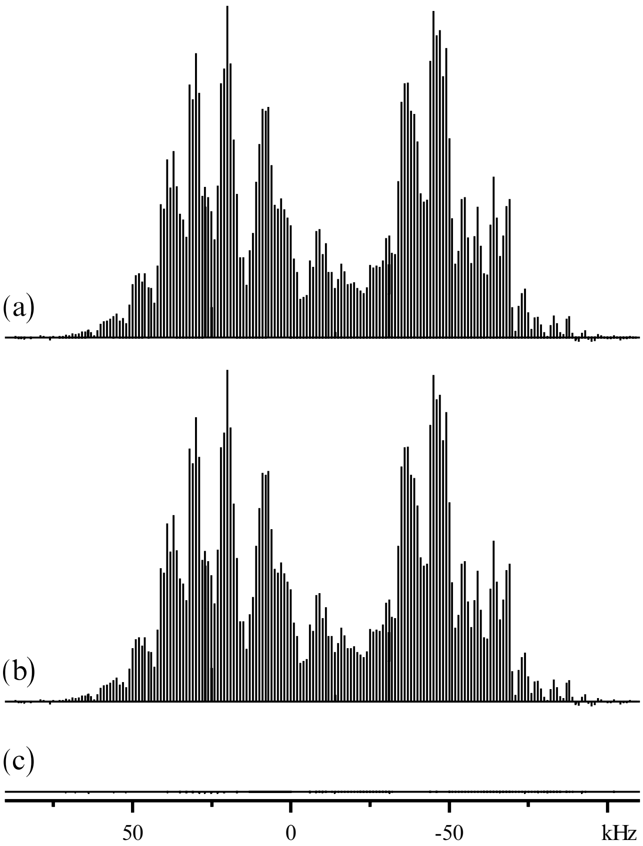

Figure 4. Theoretical spectra (stick plots of integrated spin–echo sideband intensities) illustrating the vanishing influence from non-secular quadrupolar second-order terms in typical QCPMG-MAS experiments influenced by finite RF pulse irradiation. The spectra were calculated using the same parameters as in figure 3(*e*) taking into account (*a*) secular and (*b*) secular as well as non-secular second-order terms (the spectra were generated using the replication method leading to figure 2(*d*)). (*c*) Difference between (*a*) and (*b*). Only 987 $\{\alpha_{CR}, \beta_{CR}\}$ angles have been used for these calculations.

requires a processing time of 1032 min while the spectrum in figure 4(*a*) requires a factor of 135 less processing time (i.e., 7.5 min).

4. Experimental

^{87}Rb QE and QCPMG-MAS spectra were recorded on Varian Unity-400 (9.4 T, 130.84 MHz for ^{87}Rb) and Unity *Plus*-750 (17.6 T, 245.42 MHz for ^{87}Rb) spectrometers equipped with homebuilt MAS probes for 5 mm rotors [30]. The experiments used spinning speeds between 9.0 kHz and 13.7 kHz controlled to ±1 Hz, a recycle delay of 4 s, and RF field strengths of 64.1 kHz (i.e., a selective $\pi/2$ pulse width of 1.95 μs) and 33.3 kHz (i.e., a selective $\pi/2$ pulse width of 3.75 μs) at 9.4 T and 17.6 T, respectively. Rb_2SO_4 and Rb_2CrO_4 were purchased from Alfa Products (Karlsruhe, Germany) and used without further purification. Numerical simulations and iterative fitting were performed on a Digital Alpha 4/1000 workstation using an MAS version of the software described in [22]. All simulations used powder averaging with 4181 pairs of $\{\alpha_{CR}, \beta_{CR}\}$ angles and 20 γ_{CR} angles. Time increments (Δt) less than 0.4 μs were employed for Dyson time ordering.

5. Results and discussion

The applicability of QCPMG-MAS NMR at high field to determine parameters for anisotropic shielding and quadrupolar coupling tensors for half-integer quadrupolar nuclei with large quadrupole couplings is addressed in this section. For this purpose we use ^{87}Rb NMR of the two rubidium salts Rb_2SO_4 and Rb_2CrO_4. The structures of Rb_2SO_4 and Rb_2CrO_4 are known to belong to the space groups *Pnam* (determined by X-ray crystallography [31]) and *Pmcn* (determined by oscillation reflection photography [32]), respectively, conforming with two crystallographically and thereby magnetically non-equivalent rubidium sites in the repeating unit. Both crystal symmetries require that the anisotropic shielding and the quadrupole coupling tensors both have one principal axis perpendicular to the mirror plane in which the Rb^+ ions are located [33], i.e., α^{σ}_{PC} and γ^{σ}_{PC} are both multiples of $\pi/2$. Parameters for the ^{87}Rb quadrupolar coupling and chemical shielding tensor determined by QCPMG-MAS NMR in this study and by other methods are listed in table 1. The precision of the parameters determined by QCPMG-MAS NMR is estimated from numerical simulations by variation of parameters.

For half-integer quadrupolar nuclei advantage may be taken of high fields to reduce quadrupolar second-order broadening, increase the effect of anisotropic shielding interactions, and reduce the demands on the RF field strength required for QCPMG-MAS NMR. Although not representing an example with very large c_Q values, these aspects are demonstrated in figure 5 by experimental and calculated high field (17.6 T, 245.42 MHz) ^{87}Rb QCPMG-MAS spectra of Rb_2SO_4. The displayed central transition region shows resolved rotational and spin–echo sideband manifolds from two ^{87}Rb sites which, according to earlier studies (table 1), are characterized by c_Q values of 2.7 MHz (left manifold) and 5.3 MHz (right manifold) [15, 34, 35]. The small and large c_Q sites are associated with chemical shielding anisotropies (δ_σ) determined previously for different values in the ranges 3–10 ppm and 23–25 ppm, respectively. Using a spinning frequency of the order of 10 kHz, it may be anticipated *a priori* that the effect of the smallest of the two shielding anisotropies largely will be averaged beyond detection $(\frac{3}{2}\delta_\sigma|\omega_0/2\pi| \ll \omega_r/2\pi)$, while effects from the largest

Table 1. Magnitudes and relative orientation of quadrupolar coupling and chemical shielding tensors for ^{87}Rb in Rb_2SO_4 and Rb_2CrO_4 determined using QCPMG-MAS NMR at 9.4 and 17.6 T.[a]

Compound	Site	Method	C_Q	η_Q	δ_σ	η_σ	δ_{iso}	α_{PC}^{σ}	β_{PC}^{σ}	γ_{PC}^{σ}	[Ref]/ Fig.
Rb_2SO_4	1	QE	2.65	0.89	−10.8	0.43	46.6	48	43	73	[35]
		MAS	2.65 ± 0.01	0.99 ± 0.01	−9 ± 4	0.36 ± 0.33	42.3 ± 0.1	−6 ± 25	62 ± 22	0 ± 88	[34]
		Single-crystal	2.72 ± 0.03	0.93 ± 0.03	2.7 ± 0.9	0.26 ± 0.62	42.6 ± 0.3	76 ± 89	17 ± 13	110 ± 37	[15]
		QCPMG-MAS	2.51 ± 0.05	0.99 ± 0.03	—	—	42.8 ± 0.5	—	—	—	5, 6
	2	QE	5.21	0.13	8.9	0.01	3.0	68	93	198	[35]
		MAS	5.31 ± 0.03	0.11 ± 0.01	−23 ± 3	0.55 ± 0.68	15.8 ± 0.2	21 ± 29	36 ± 8	77 ± 44	[34]
		Single-crystal	5.29 ± 0.05	0.12 ± 0.03	−25 ± 3	0.54 ± 0.30	15.5 ± 1.6	9 ± 26	37 ± 5	270 ± 22	[15]
		QCPMG-MAS	5.21 ± 0.1	0.09 ± 0.03	−27 ± 4	0.69 ± 0.40	16.2 ± 0.5	34 ± 30	42 ± 10	268 ± 40	5, 6
Rb_2CrO_4	1	QE	11.53	0.75	13.1	0.16	52.8	−77	74	0	[35]
		Single-crystal	9.43 ± 0.66	0.700 ± 0.014	−80 ± 7	0.19 ± 0.14	−60 ± 3	90[b]	−0.9 ± 1.9	0[b]	[16]
		QCPMG-MAS	9.50 ± 0.1	0.68 ± 0.05	−69 ± 20	0.75 ± 0.50	−56 ± 4	90[b]	28 ± 30	0[b]	8, 9
	2	QE	5.23	0.48	149.2	0.25	−47.4	37	−15	28	[35]
		SAS	3.5	0.3	110	0.0	−7	—	70	0	[10]
		Single-crystal	3.549 ± 0.014	0.362 ± 0.012	109.7 ± 0.6	0.037 ± 0.010	−8.7 ± 0.2	93 ± 11	68.88 ± 0.16	−0.3 ± 1.6	[16]
		QCPMG-MAS	3.56 ± 0.05	0.36 ± 0.03	103 ± 10	0.0[b]	−7.5 ± 0.5	0[b]	62 ± 10	15 ± 30	8, 9

[a] The quadrupolar coupling (C_Q) is in MHz, the isotropic chemical shift (δ_{iso}) and the chemical shielding anisotropy (δ_σ) in ppm, and the Euler angles $(\alpha_{PC}^{\sigma}, \beta_{PC}^{\sigma}, \gamma_{PC}^{\sigma})$ in deg. Shifts are given on the δ scale relative to 1.0 M $RbNO_3$. Precisions for parameters determined from QCPMG-MAS NMR are estimated using numerical simulations by variation of parameters.

[b] Parameters fixed during optimization.

shielding tensor potentially may be visible using the 17.6 T magnetic field ($\frac{3}{2}\delta_\sigma|\omega_0/2\pi| \sim 9.2$ kHz). It is still, however, an open question how small shielding anisotropies actually can be detected under these conditions when considering all spectral features including those of low-sensitivity spinning sidebands being easier to retrieve through their splitting into spin–echo sidebands using QCPMG-MAS NMR relative to QE-MAS NMR.

With an available RF field strength of 33.3 kHz, $|\omega_Q/\omega_{RF}| > 3.5$ and $2\omega_Q^2/(\omega_0/\omega_{RF}) < 0.05$ suggesting that the experimental spectrum of Rb_2SO_4 (figure 5(*a*), vertical expansion in figure 5(*d*)) may be analysed by simulations within the ideal RF pulse approximation. Considering the large C_Q site, it is evident from the simulation resulting from iterative fitting of the experimental spectra (figure 5(*b*, *e*), parameters in table 1) plus the simulation using the same parameters but $\delta_\sigma = 0$ (figure 5(*c*, *f*)) that the QCPMG-MAS spectrum of Rb_2SO_4 allows detection of effects from both the quadrupole coupling and the small anisotropic shielding interactions. This becomes particularly evident from the vertical expansions in figure 5(*d*–*f*) of the spin–echo sideband manifolds from the spinning sidebands. Addressing the small C_Q site, it is not possible at this spinning speed to identify any influence from anisotropic shielding even using a high magnetic field strength. Using the same experimental setup at 9.4 T it becomes difficult to detect effects from anisotropic shielding even for the large C_Q site, which is in full accord with *a priori* expectations. This is demonstrated by the experimental and simulated spectra in figure 6.

An intriguing test of the performance of QCPMG-MAS experiments in cases of large C_Q's is the ^{87}Rb NMR of Rb_2CrO_4. This compound has been studied previously using a variety of experimental methods including DAS [17], SAS [10], MQMAS [18], static-sample QE [35], and single-crystal [16] NMR (parameters included in table 1). We note that only the QE and single-crystal studies have provided parameters for the ^{87}Rb site with the largest quadrupole coupling (i.e., $C_Q \sim 10$ MHz) characterized by a second-order powder pattern for the central-transition centreband being more than 100 kHz wide at 9.4 T.

Figure 7 shows a series of ^{87}Rb QCPMG-MAS spectra recorded at 9.4 T along with the corresponding QE-MAS spectrum included to demonstrate the gain in sensitivity that may be achieved by recording the FID in the course of a train of spin–echo refocusing pulses. By adjusting the π interpulse spacing, it is possible to balance the actual sensitivity gain against the digitization of the spectral information. For the spectra in figure 7(*b*, *c*, *d*) the spin–echo sideband splitting is 0.5, 1, and 2 kHz, respectively, leading to sensitivity gain factors of 14, 18 (46), and 28 (138) relative to that of the QE-MAS spectrum (figure 7(*a*)). These factors are all corrected to correspond to a dwell time of 5 μs. Without this adjustment the gain factors in parentheses apply. Besides the direct advantage of the significantly improved sensitivity, it should be noted that QCPMG-MAS through splitting of the powder patterns into distinct sidebands facilitates discrimination of broad second-order powder patterns from background and baseline artefacts. This is

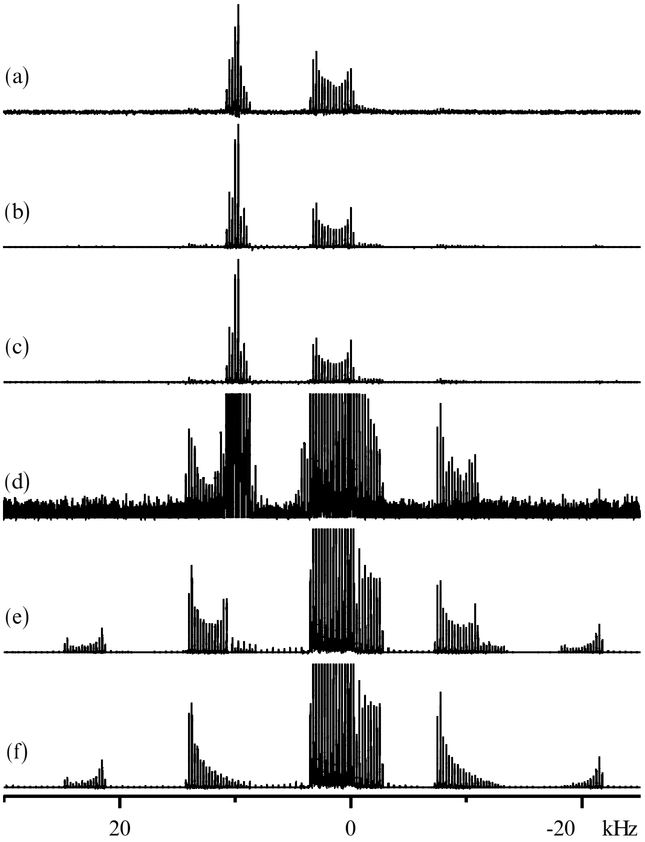

Figure 5. 17.6 T (245.42 MHz) ^{87}Rb QCPMG-MAS spectra of Rb$_2$SO$_4$. (*a*) Experimental spectrum recorded using $\omega_r/2\pi = 10\,765$ Hz, $\tau_1 = 89.15\ \mu s$, $\tau_2 = 92.9\ \mu s$, $\tau_3 = 40.0\ \mu s$, $\tau_a = 4.0$ ms, $M = 30$, $\tau_d = 9.072$ ms, a dwell time of 8 μs, and 1024 scans. (*b*) Calculated spectrum using the parameters in table 1 obtained through iterative fitting of the experimental spectrum in (*a*) under the assumption of ideal RF pulses (see text). (*d*) and (*e*) are vertical expansions (by a factor 30) of the spectra in (*a*) and (*b*), respectively. The calculated spectrum (*c*) and its vertically expanded analogue (*f*) used the same parameters as in (*b*) and (*e*), but with $\delta_\sigma = 0$. The experimental and calculated spectra were apodized using 1 Hz and 10 Hz Lorentzian line broadening, respectively.

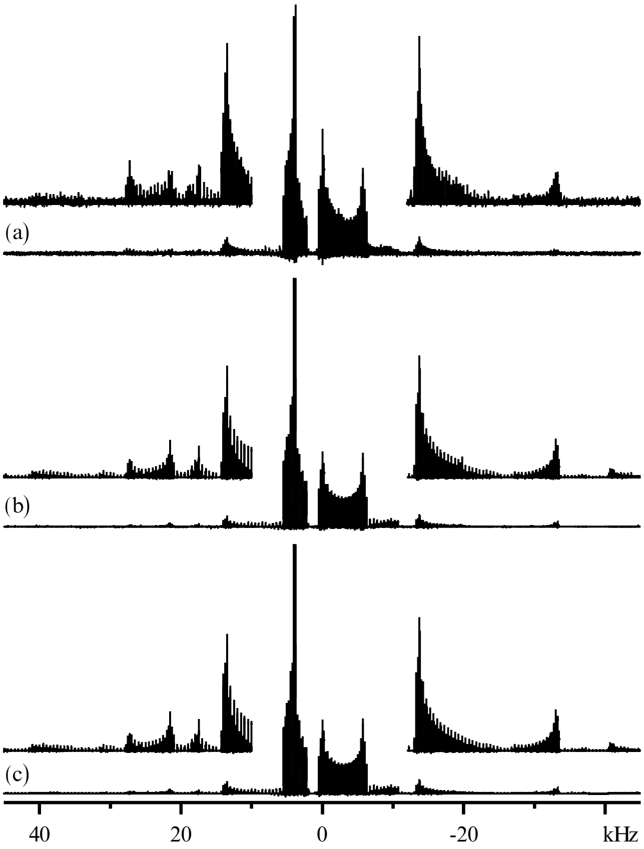

Figure 6. 9.4 T (130.84 MHz) ^{87}Rb QCPMG-MAS spectra of Rb$_2$SO$_4$. (*a*) Experimental spectrum recorded using $\omega_r/2\pi = 13\,645$ Hz, $\tau_1 = \tau_2 = 71.3\ \mu s$, $\tau_3 = 50.0\ \mu s$, $\tau_a = 4.0$ ms, $M = 19$, $\tau_d = 3.92$ ms, a dwell time of 10 μs, and 128 scans. (*b*) Simulated spectrum corresponding to the parameters in table 1 obtained by iterative fitting under the assumption of ideal RF pulses. (*c*) Simulated spectrum using the same parameters as (*b*) but with $\delta_\sigma = 0$. The inserts are scaled by a factor 10 in the vertical direction. Experimental and calculated spectra were apodized using 1 Hz and 10 Hz Lorentzian line broadening, respectively.

evident particularly in the region from say −50 kHz to −90 kHz.

Addressing extraction of parameters for the anisotropic shielding and quadrupolar coupling tensors, figures 8 and 9 show ^{87}Rb QCPMG-MAS spectra of Rb$_2$CrO$_4$ corresponding to magnetic fields of 9.4 T and 17.6 T, respectively. To obtain sufficient spectral information for both sites, characterized by widely different quadrupolar couplings (see table 1), the spin–echo sideband separation has been adjusted to 500 Hz and 250 Hz at 9.4 T and 17.6 T, respectively, considering different scaling of the two interactions by the external field. In both figures the experimental spectrum is shown in (*a*), a simulation resulting from optimum fitting of the two experimental spectra considering finite RF pulse performance in (*b*), while (*c*) and (*d*) show individual simulations of the two ^{87}Rb sites in Rb$_2$CrO$_4$. The optimum parameters for the anisotropic interactions are given in table 1. The favourable agreement between experimental and simulated spectra under both fields and the acceptable match between the corresponding parameters and those determined by single-crystal NMR [16] demonstrate that heavy overlap of centrebands and spinning sidebands from the two sites does not prevent extraction of reliable parameters from the QCPMG-MAS spectra. To a large extent this is ascribed to the possibility of identifying weak spin–

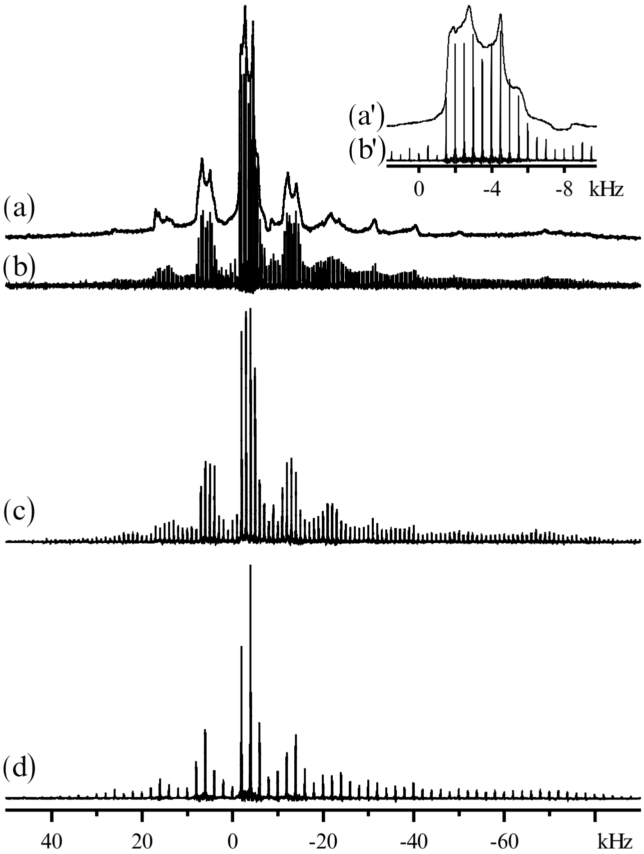

Figure 7. Experimental ^{87}Rb (*a*) QE-MAS and (*b–d*) QCPMG-MAS spectra of Rb_2CrO_4 at 9.4 T (130.84 MHz). The spectra were recorded using: (*a*) $\omega_r/2\pi = 8506$ Hz, $\tau_1 = \tau_2 = 103.25$ μs, a dwell time of 5 μs, and 1024 transients; (*b*) $\omega_r/2\pi = 9506$ Hz, $\tau_1 = \tau_2 = 103.25$ μs, $\tau_a = 2.0$ ms, $M = 19$, $\tau_d = 1.96$ ms, and a dwell time of 5 μs; (*c*) $\omega_r/2\pi = 9059$ Hz, $\tau_1 = \tau_2 = 108.4$ μs, $\tau_a = 1.0$ ms, $M = 15$, $\tau_d = 1768$ ms, and a dwell time of 2 μs; and (*d*) $\omega_r/2\pi = 9935$ Hz, $\tau_1 = \tau_2 = 98.7$ μs, $\tau_a = 0.5$ ms, $M = 15$, $\tau_d = 1768$ ms, and a dwell time of 1 μs. All the QCPMG-MAS spectra used $\tau_3 = 50.0$ μs and 128 transients. The inserts (a', b') show horizontal expansions of the central region of the spectra (a, b). The spectra are apodized using Lorentzian linebroadening of (*a*) 1, (*b*) 5, (*c*) 50, and (*d*) 75 Hz, respectively. Going from (*a*) to (*d*) the vertical scale was reduced by factors 1, 14, 18, and 28.

echo sidebands from the broad powder patterns of the high C_Q site 1.

One way to avoid overlap between centrebands and spinning sidebands is to combine the QCPMG-MAS experiment with the QPASS experiment [36]. This provides high sensitivity along with the advantage of MAS with infinite spinning frequency. To explore this approach, figure 8(*e*) shows a simulated 9.4 T ^{87}Rb QCPMG-MAS spectrum assuming infinite spinning speed and ideal RF pulse excitation. In this spectrum the centrebands are clearly separated although at the expense of lost information about the anisotropic shielding interaction.

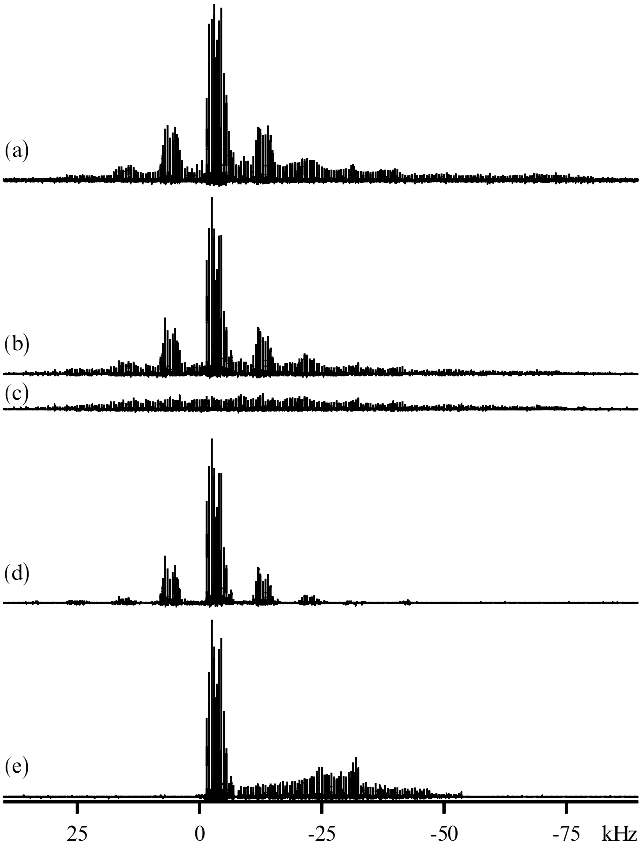

Figure 8. Experimental and simulated ^{87}Rb QCPMG-MAS spectra of Rb_2CrO_4 at 9.4 T (130.84 MHz). The experimental spectrum (*a*) is identical to the spectrum in figure 7(*b*). The simulated spectra in (*b–d*) were calculated using the experimental parameters of (*a*) and parameters obtained from optimum iterative fitting (assuming finite RF pulses) as given in table 1. Spectrum (*b*) shows sideband manifolds from both sites while (*c*) and (*d*) give those from sites 1 and 2, individually. The simulated spectrum in (*e*) uses the same parameters as (*b*) but assumes ideal excitation with spinning frequency of 250 kHz. The spectra were apodized using Lorentzian linebroadenings of (*a*) 1, (*b*) 5, and (*c–e*) 10 Hz.

6. Conclusion

We have demonstrated that the QCPMG-MAS experiment may provide a gain in sensitivity by an order of magnitude (about 30 in the present experiments) while allowing determination of magnitudes and relative orientation of quadrupolar coupling and anisotropic shielding interactions. For large quadrupolar interactions the spectral simulations require consideration of finite RF pulse excitation while non-secular

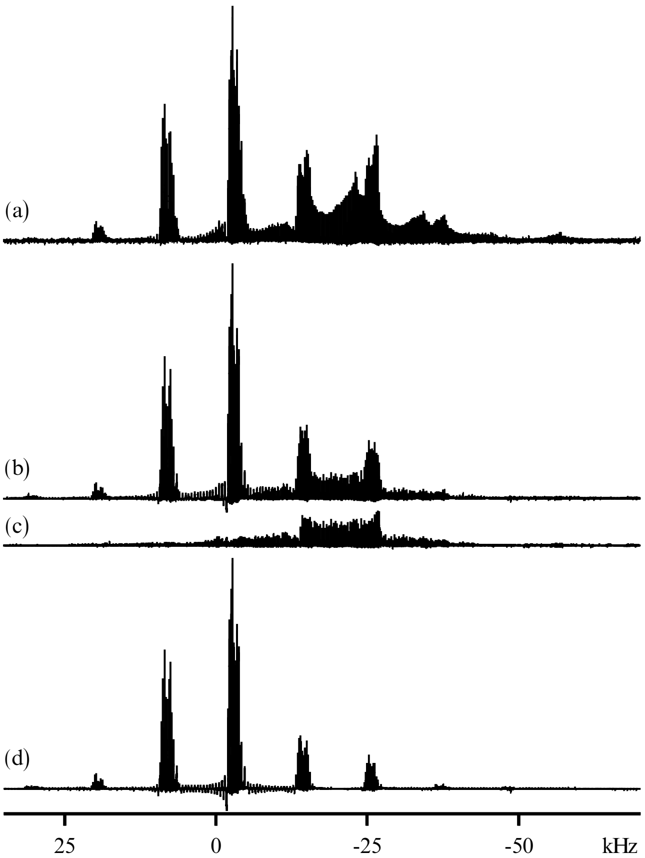

Figure 9. ^{87}Rb QCPMG-MAS spectra of Rb_2CrO_4 at 17.6 T (245.42 MHz). (*a*) Experimental spectrum recorded using $\omega_r/2\pi = 11\,254$ Hz, $\tau_1 = 85.1\ \mu s$, $\tau_2 = 88.85\ \mu s$, $\tau_3 = 40.0\ \mu s$, $\tau_a = 4.0$ ms, $M = 15$, $\tau_d = 3.54$ ms, a dwell time of 4 μs, and 1024 transients. (*b–d*) Simulated spectra corresponding to the parameters in table 1 and finite RF pulses, with sideband manifolds from (*b*) both sites, (*c*) site 1, and (*d*) site 2.

second-order terms of the quadrupolar interaction do not influence the spin evolution appreciably. Considering these aspects the applicability of the QCPMG-MAS experiment has been demonstrated by ^{87}Rb spectra of Rb_2SO_4 and Rb_2CrO_4 in the present study. Based on the results from this analysis, it is envisaged that the QCPMG-MAS NMR may find important applications in the study of quadrupolar nuclei with low receptivity and large quadrupolar coupling interactions.

The use of the Varian Unity-400 spectrometer, sponsored by Teknologistyrelsen, at the Instrument Centre for Solid-State NMR Spectroscopy, University of Aarhus is acknowledged. Support of this research by equipment grants from the Danish Natural Science Foundation Council, Carlsbergfondet, and Aarhus University Research Foundation is acknowledged. This work has been supported in part by the National Institutes of Health under a Related Services Agreement with the US Department of Energy (DOE) under Contract DE-AC06-76RLS1830, Federal Grant 8-R1GM26295F. Pacific Northwest National Laboratory is operated for DOE by Batelle. The authors thank Dr A. S. Lipton for technical assistance.

References

[1] Samoson, A., and Lippmaa, E., 1983, *Phys. Rev. B*, **28,** 6567.

[2] Kentgens, A. P. M, Lemmens, J. J. M., Geurts, F. M. M., and Veeman, W. S., 1987, *J. magn. Reson.*, **71**, 62.

[3] Nielsen, N. C., Bildsøe, H., Jakobsen, H. J., 1992, *J. magn. Reson.*, **97**, 149.

[4] Jakobsen, H. J., Skibsted, J., Bildsøe, H., and Nielsen, N. C., 1989, *J. magn. Reson.*, **85,** 173.

[5] Skibsted, J., Nielsen, N. C., Bildsøe, H., and Jakobsen, H. J., 1992, *Chem. Phys. Lett.*, **188,** 405.

[6] Mueller, K. T., Sun, B. Q., Chingas, G. C., Zwanzinger, J. W., Terao, T., and Pines, A., 1990, *J. magn. Reson.*, **86,** 470.

[7] Samoson, A., Lippmaa, E., and Pines, A., 1988, *Molec. Phys.*, **65,** 1013.

[8] Samoson, A., and Pines, A., 1989, *Rev. sci. Instrum.*, **60,** 3239.

[9] Wu, Y., Sun, B. Q., Pines, A., Samoson, A., and Lippmaa, E., 1990, *J. magn. Reson.*, **89,** 297.

[10] Shore, J. S., Wang, S. H., Taylor, R. E., Bell, A. T., and Pines, A., 1996, *J. chem. Phys.*, **105,** 9412.

[11] Frydman, L., and Harwood, J. S., 1995, *J. Amer. chem. Soc.*, **117,** 5367.

[12] Wu, G., Rovnyak, D., Sun, B., and Griffin, R. G., 1995, *Chem. Phys. Lett.*, **249,** 210.

[13] Fernandez, C., and Amoureux, J.-P., 1995, *Chem. Phys. Lett.*, **242,** 449.

[14] Vosegaard, T., Larsen, F. H., Jakobsen, H. J., Ellis, P. D., and Nielsen, N. C., 1997, *J. Amer. chem. Soc.*, **119,** 9055.

[15] Vosegaard, T., Skibsted, J., Bildsøe, H., and Jakobsen, H. J., 1996, *J. magn. Reson. A*, **122,** 111.

[16] Vosegaard, T., Byriel, I. P., and Jakobsen, H. J., 1997, *J. phys. Chem. B*, **101,** 8959.

[17] Baltisberger, J. H., Gan, S. L., Wooten, E. W., Chang, T. H., Mueller, K. T., and Pines, A., 1992, *J. Amer. chem. Soc.*, **114,** 7489.

[18] Wang, S. H. Xu, Z., Baltisberger, J. H., Bull, L. M., Stebbins, J. F., and Pines, A., 1997, *Solid State nucl. magn. Reson.*, **8,** 1.

[19] Solomon, I., 1958, *Phys. Rev.*, **110,** 61.

[20] Weisman, I. D., and Bennett, L. H., 1969, *Phys. Rev.*, **181,** 1341.

[21] Davis, J. H., Jeffrey, K. R., Bloom, M., Valic, M. I., and Higgs, T. P., 1976, *Chem. Phys. Lett.*, **42,** 390.

[22] Larsen, F. H., Jakobsen, H. J., Ellis, P. D., and Nielsen, N. C., 1997, *J. phys. Chem. A*, **101,** 8597.

[23] Larsen, F. H., Jakobsen, H. J., Ellis, P. D., and Nielsen, N. C., 1998, *J. magn. Reson.*, **131,** 144.

[24] Carr, H. Y., and Purcell, E. M., 1954, *Phys. Rev.*, **94,** 630.

[25] Meiboom, S., and Gill, D., 1958, *Rev. sci. Instrum.*, **29,** 688.

[26] Dyson, F. J., 1949, *Phys. Rev.*, **75,** 486.

[27] Zaremba, S. K., 1966, *Annali Mat. pura appl.*, **73,** 293.

[28] Abragam, A., 1961, *The Principles of Nuclear Magnetism* (Oxford: Clarendon Press).

[29] Nielsen, N. C., Bildsøe, H., and Jakobsen, H. J., 1992, *Chem. phys. Lett.*, **191,** 205.

[30] Jakobsen, H. J., Daugaard, P., and Langer, V., 1988, *J. magn. Reson.*, **76,** 162.

[31] Nord, A. G., 1974, *Acta Crystallogr. B*, **30,** 1640.

[32] Smith, H. W., and Colby, M. Y., 1940, *Z. Kristallogr.*, **103,** 90.

[33] Weil, J. A., Buch, T., and Clapp, J. E., 1973, *Adv. magn. Reson.*, **8,** 183.

[34] Fernandez, C., Amoureux, J.-P., Bodart, P., and Maijanen, A., 1995, *J. magn. Reson. A*, **113,** 205.

[35] Cheng, J. T., Edwards, J. C., and Ellis, P. D., 1990, *J. phys. Chem.*, **94,** 553.

[36] Massiot, D., Montouillout , V., Fayon, F., Florian, P., and Bessada, C., 1997, *Chem. phys. Lett.*, **272,** 295.